Key Engineering Materials
ISSN: 1662-9795, Vol. 1047, pp 41-51

Submitted: 2025-12-17
Revised: 2026-02-17
Accepted: 2026-02-25
Online: 2026-04-13

Numerical Modelling of Directed Energy Deposition and Experimental Validation Based on Digital Image Correlation

Dejan Kovšca[1,a], Bojan Starman[1,b], Edvard Govekar[1,c], Miroslav Halilovič[1,d] and Nikolaj Mole[1,e*]

[1]Faculty of Mechanical Engineering, University of Ljubljana, Ljubljana, Slovenia

[a]dejan.kovsca@fs.uni-lj.si, [b]bojan.starman@fs.uni-lj.si, [c]edvard.govekar@fs.uni-lj.si, [d]miroslav.halilovic@fs.uni-lj.si, [e]nikolaj.mole@fs.uni-lj.si

[*]corresponding author

Keywords: directed energy deposition, laser cladding, finite element method, digital image correlation.

Abstract. This contribution presents a combined approach for in-situ experimental characterisation and numerical modelling of thermo-mechanical behaviour in directed energy deposition (DED). Full-field temperature and substrate deformation are measured simultaneously using infrared (IR) thermography and stereo digital image correlation (DIC) during laser-beam powder deposition on a thin substrate. The experimental data are used to calibrate thermal boundary conditions and to validate a macroscopic finite-element model. The validated framework is then applied to compare different deposition strategies, demonstrating the capability of the coupled measurements and simulations to capture transient thermal fields, deformation evolution and toolpath-dependent effects relevant for process optimisation.

Introduction

Additive manufacturing (AM) is increasingly used to produce complex metal components, yet the steep thermal gradients and rapid solidification inherent to the process often lead to residual stresses, distortion, and reduced dimensional accuracy. Numerical simulations are therefore widely employed to predict thermal histories and mechanical responses and to support process optimisation, but their predictive capability depends strongly on high-quality experimental data for model calibration and validation [1].

Thermal measurements in metal AM traditionally rely on thermocouples, which offer robust but point-based observations [2]. Infrared (IR) thermography provides a contactless alternative with full-field capability, though its accuracy is influenced by varying surface emissivity. Several studies have addressed these limitations through emissivity calibration or indirect viewing strategies, such as mirror-based observation of concealed surfaces [3],[4].

Similarly, deformation monitoring has progressed from single-point probes and displacement sensors [5] to optical full-field methods. Digital image correlation (DIC) has emerged as particularly suitable for AM because it enables non-contact measurement of full-field 3D displacements and strains by correlating sequential stereo images [6]–[8]. Despite its potential, in-situ DIC remains challenging due to illumination constraints, speckle-pattern degradation, and obstructions from the deposition process [9].

To address the need for reliable, continuous in-situ data, this study introduces an experimental methodology that combines IR thermography with stereo DIC for simultaneous full-field measurement of temperature and substrate deformation during directed energy deposition (DED). This coupled dataset is used to validate a macroscopic thermo-mechanical finite-element model. The paper describes the numerical framework, experimental setup, and in-situ measurement procedure, followed by thermal-boundary-condition calibration. The influence of deposition strategy on the thermal response, residual stresses, and deformation is then evaluated.

Experimental Study

To assess the reliability of the numerical model, three representative toolpaths were deposited while monitoring both the thermal evolution and the resulting substrate deformation in-situ. For this purpose, an integrated measurement setup was developed that simultaneously records IR temperature data and out-of-plane displacement fields via a stereo DIC system.

Experimental setup. Material deposition was performed on a laboratory DED system equipped with an nLIGHT CMP-2500 continuous fibre laser with a maximum average power of 2.5 kW, a disc powder feeder and a custom annular cladding head with axial powder injection. Argon served as the carrier and shielding gas. Motion was provided by a CNC-controlled positioning table, allowing deposition within a 200 × 60 × 120 mm build volume.

The substrate was fixed to a water-cooled AA6061 mounting frame. The frame was elevated and contains a 100 × 100 mm opening, enabling direct optical access to the bottom surface of the substrate during processing, as shown in Fig. 1a.

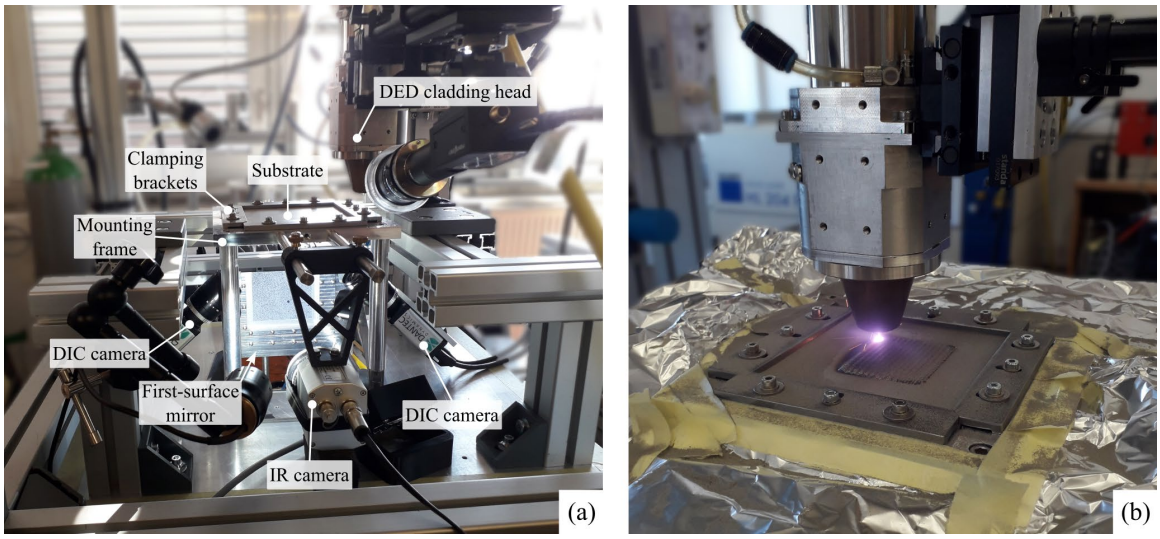

Fig. 1. (a) The experimental setup consists of the experimental DED system and an elevated mounting frame. The substrate is fixed using clamping brackets. IR camera and a pair of digital cameras for stereo DIC are positioned on the side of the mounting frame. Subfigure (b) shows the experimental setup during the deposition process, with the measuring equipment protected by a layer of aluminium foil.

Surface deformation was measured using a stereo DIC system consisting of two Manta G-201B 5 Mpx digital cameras arranged to provide full coverage of the visible region. A high-contrast speckle pattern was applied using heat-resistant spray paint (thermally stable up to 800 °C) on the bottom surface of the substrate, as shown in Fig. 2d, and the system was calibrated with a 5 × 5 mm target. Displacement fields were evaluated in Dantec Dynamics Istra 4D software from images acquired at 1 Hz. All optical equipment beneath the deposition area was shielded from spatter and radiation using a layer of thin aluminium foil, as seen in Fig. 1b.

The transient thermal field on the underside of the substrate was captured by an Optris PI640 IR camera, operated via the Optris PIX Connect software, positioned to view the surface through a first-surface mirror integrated beneath the frame at a 45° angle. Measurements were performed in the temperature range of 150–900 °C at 10 Hz. Temperature evaluation was conducted directly on the DIC speckle coating. Consequently, the deposition of new beads on the opposite side of the substrate and any associated surface oxidation did not influence the IR temperature measurements. The emissivity of this painted surface was calibrated against a reference K-type thermocouple and determined to be 0.9. No variation in thermal response or visible degradation of the coating was observed during the process; therefore, the emissivity was considered constant throughout the experiments.

Deposition process.

The experiments were performed using AISI 316L powder deposited onto a hot-rolled AISI 304L substrate plate with dimensions of 120 × 120 mm and a thickness of 3 mm. The chemical compositions of both alloys, as provided by the manufacturers, are listed in Table 2. Key process parameters applied in all experiments are summarised in Table 1.

Table 1. Process parameters used in the experimental case studies.

Parameter	Value
Laser beam power [W]	1000.0
Laser beam diameter [mm]	3.4
Working move velocity [mm/min]	300.0
Positioning velocity [mm/min]	900.0
Powder mass flow rate [g/min]	8.0
Shielding gas volume flow [L/min]	8.0
Powder carrier gas volume flow [L/min]	0.5
Cooling water temperature [K]	292.0

Prior to deposition, the substrate was clamped to the water-cooled mounting frame using twelve uniformly preloaded M4 screws tightened to a torque of 0.8 Nm to ensure deterministic boundary conditions. Sufficient time was allowed for the assembly to reach thermal equilibrium before and after the deposition process.

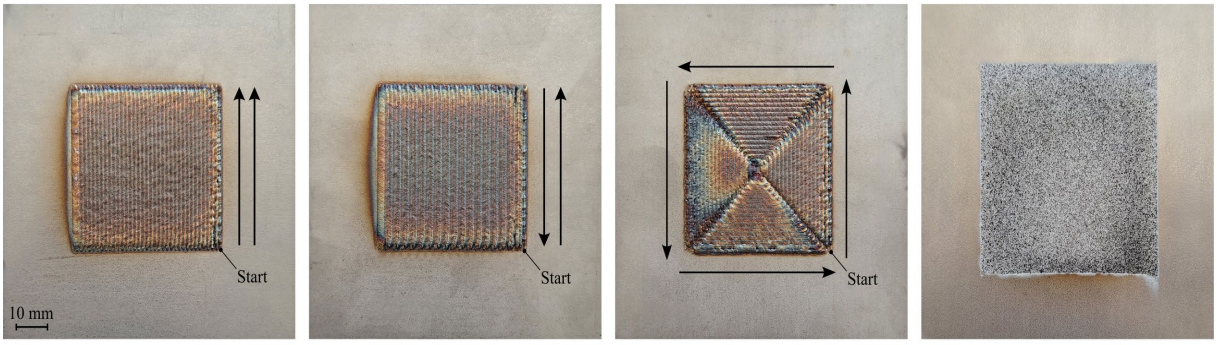

(a) Unidirectional path (b) Bidirectional path (c) Inward-spiral path (d) DIC speckle pattern

Fig. 2. Final deposits were manufactured using three distinct deposition strategies: (a) unidirectional, (b) bidirectional, and (c) inward-spiral. Subfigure (d) shows the speckle pattern applied to the underside of the substrate.

Three representative deposition-path strategies were investigated, each producing a deposition region of approximately 60 × 60 mm, as shown in Fig. 2a-c:

- *Unidirectional deposition path:* 36 parallel beads were deposited in the same direction, with a centre-to-centre spacing of 1.68 mm. Each bead was deposited in approximately 11.7 s, followed by a 5.5 s dwell time while the cladding head repositioned to the starting point for the next path, resulting in a total processing time of 612 s.
- *Bidirectional deposition path:* The same geometric pattern was used as in the unidirectional case, but the scan direction alternated after each bead. Interpass delays were kept identical to the unidirectional case, so the overall processing time remained unchanged.
- *Inward-spiral deposition path:* 17 concentric perimeters were deposited from the outer edge inward, maintaining the same bead overlap as in the linear strategies. This approach reduced traveling motion, yielding a total processing time of 500 s.

Numerical Model Implementation

The thermo-mechanical analysis follows a weakly coupled strategy in which the thermal and mechanical problems are solved sequentially, consistent with earlier work by Kovšca et al. [10]. A transient 3D thermal simulation is performed first using a calibrated heat-source model, and the resulting nodal temperatures are then applied as loads in a quasi-static mechanical analysis. The mechanical response is evaluated using a thermo-elasto-plastic material model, capturing temperature-dependent softening and plastic deformation induced by non-uniform thermal expansion.

Material deposition is represented through the incremental activation of finite elements following the hybrid inactive/quiet approach proposed by Michaleris [11]. Initially elements are added to the computational domain bead by bead, assigned with modified properties that prevent interaction with the active mesh. Upon activation, they are updated with the correct thermo-mechanical material properties. Activation times are precomputed using an in-house routine based on the toolpath and process parameters. To account for the evolving free surface, a boundary-detection algorithm from Kovšca et al. [10] is used to update heat-loss conditions as the build progresses. The simulation framework is implemented in Abaqus/Standard (2024), using implicit time integration with geometric nonlinearity enabled and customised subroutines for element activation and thermal boundary-condition control.

Material properties.

Temperature-dependent material data for both the 316L powder and the 304L substrate, shown in Fig. 3, were generated using JMatPro (version 14.0), based on the certified chemical compositions presented in Table 2. The material model assumes homogeneous, isotropic behaviour. Melting and solidification effects are included through latent heat at the solidus and liquidus temperatures listed in Table 3. Temperature-dependent isotropic hardening follows the constitutive description of Muránsky et al. [12]. Although a mixed isotropic–kinematic hardening model would provide a more accurate representation of cyclic plasticity under repeated thermal loading and could improve residual stress and springback predictions, isotropic hardening was selected to limit computational cost. Given the dense mesh and full-process simulation of the deposition sequence, the use of a mixed hardening formulation would substantially increase solution time and was therefore not considered feasible within the available computational resources.

Table 2. Chemical composition [wt. %] of AISI 316L and AISI 304L material.

Material	C	Cr	Mn	Mo	N	Ni	P	S	Si	Fe
304L	0.023	18.02	1.814	-	0.072	8.040	0.028	0.001	0.361	bal.
316L	0.020	17.30	1.740	2.660	-	13.10	-	< 1.0	0.730	bal.

Table 3. Phase change properties of AISI 316L and AISI 304L material.

Parameter	Symbol	AISI 304L	AISI 316L
Solidus temperature [K]	T_S	1676.1	1683.7
Liquidus temperature [K]	T_L	1733.6	1710.3
Latent heat of fusion [kJ/kg]	L_f	174.9	180.2

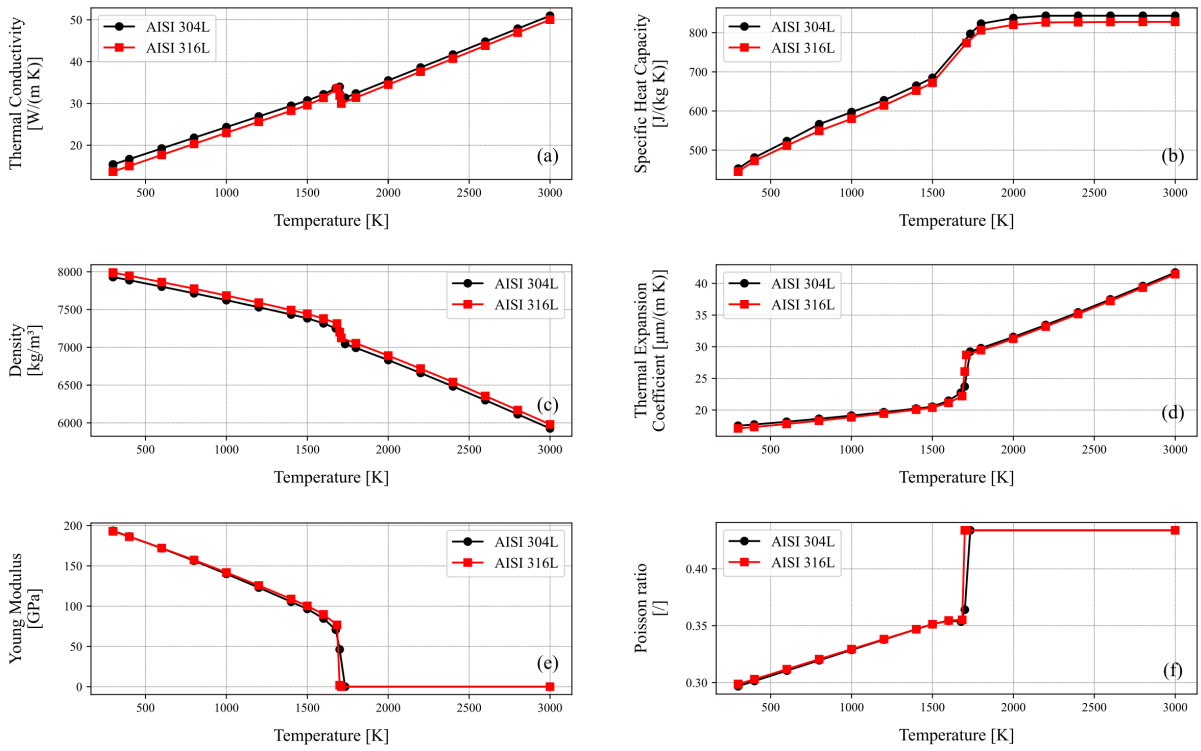

Fig. 3. Temperature-dependent material properties of AISI 316L and AISI 304L material.

Finite element mesh.

Accurate modelling of the bead profile is essential, as the deposited volume directly governs the heat input and thus the thermo-mechanical response of the substrate, as demonstrated by Santi et al. [13]. Although a realistic bead shape improves accuracy, it requires dense, case-specific meshing, making it impractical for studies on deposition-pattern or toolpath optimisation. For this reason, an area-equivalent rectangular bead representation is commonly adopted, offering simpler meshing and improved computational efficiency. In the present study, the bead width (w) is defined by the path offset distance (p) as 1.68 mm, while the bead height (h), determined from deposited volume conservation, equals 0.9186 mm.

This representation introduces sharp corners at the bead–substrate interface, which may locally increase thermal gradients and affect the local stress distribution compared to a parabolic bead profile. However, since the deposited area and heat input are preserved and the focus is on the global thermo-mechanical response of the substrate, particularly on its bottom surface, the simplification is considered acceptable within the scope of the study.

The numerical model replicates the real geometry of the substrate, brackets, and mounting frame used in the experiments. All deformable solid regions use eight-node hexahedral elements, with DC3D8 elements employed for the thermal analysis and C3D8 elements for the mechanical analysis. The mounting frame is modelled as a rigid body using R3D4 surface elements. The rectangular bead profile is represented by a 3×3 element layout, while the substrate mesh is gradually coarsened toward the edges and consists of four elements through the thickness, as shown in Fig. 4. The complete model contains 53,352 elements for the substrate and filler material, 2,112 elements for the mounting frame and 1,562 elements for each of the four clamping brackets.

Heat source model. During DED, molten filler material is continuously added along the toolpath, producing strong local heating and phase changes. In the simulation, this behaviour is captured by activating quiet elements once they reach the melting temperature T_{melt}, meaning that the heat source accounts only for the excess energy transferred to the substrate. The volumetric power distribution follows the ellipsoidal model of Goldak et al. [14], as given by Eq. (1).

$$Q(x,y,z) = \frac{6\sqrt{3}\,P\,\eta_{sys}\,\alpha_{sub}\,f_{sub}}{\pi\sqrt{\pi}\,a\,b\,c}\,\exp\left(-3\left(\frac{x^2}{a^2}+\frac{y^2}{b^2}+\frac{z^2}{c^2}\right)\right), \quad (1)$$

where P is the nominal laser source power, whereas a, b and c define the semi-axes of the ellipsoid along the x, y and z directions, respectively. The heat-source efficiency combines system losses η_{sys}, substrate absorptivity α_{sub}, and the fraction of power absorbed in substrate that does not contribute to melting of the filler material f_{sub}.

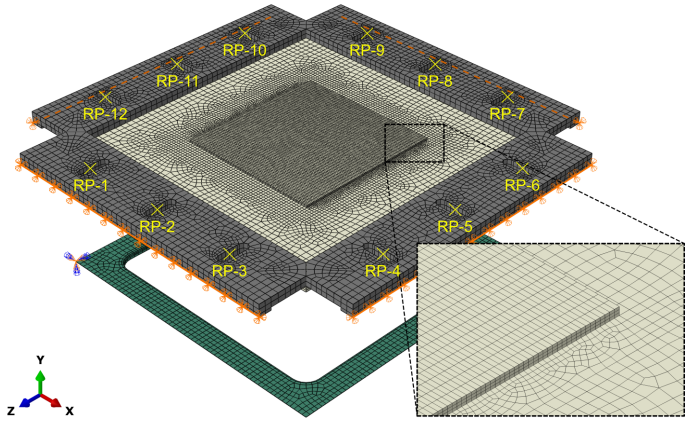

Fig. 4. Finite element mesh of the substrate and beads (white), clamps (grey), and rigid mounting frame (green). Preload is applied to the clamps via spring elements at the reference points (RP). Hinge constraints (orange) are imposed on the clamps, the mounting frame is fully constrained, while the substrate is restrained only by contact interactions.

For the present DED system, the heat-source semi-axes a, b, and c correspond to a four-sigma laser-spot diameter of 3.4 mm and a measured melt-pool penetration depth of 0.45 mm, with approximately 25% of the nominal laser power lost within the deposition head. The complete parameter set is listed in Table 4.

Table 4. Heat source parameters used in the numerical case studies.

Parameter	Symbol	Value
Nominal laser power [W]	P	1000.0
Laser beam radius [mm]	a, b	1.700
Laser beam penetration depth [mm]	c	0.450
Cladding system efficiency [/]	η_{sys}	0.750
Substrate absorptivity coefficient [/]	α_{sub}	0.360
Heat fraction transferred to substrate [/]	f_{sub}	0.693

Thermal boundary conditions.

In the thermal model, only the substrate and deposited beads are represented explicitly, while the influence of the clamps and mounting frame is accounted for through an equivalent heat-loss boundary condition. The model also includes radiation and free convection on the substrate surface.

To determine the relevant heat-transfer coefficients, two cooldown experiments were performed: one with the substrate supported on tips to capture free convection, and one with the substrate clamped to the water-cooled mounting frame to characterise conductive heat loss. Emissivity values were identified by comparing thermal images with thermocouple measurements, resulting in 0.3 for the substrate surface and 0.9 for the speckle pattern. These surface emissivity values are also applied in the Stefan–Boltzmann radiation model.

Each cooldown experiment begins by uniformly heating the substrate and recording the subsequent cooling behaviour. The temperature field at the moment heating is stopped is processed and mapped onto a numerical mesh to initialise a steady-state analysis in Abaqus. Transient simulations are then

conducted over a range of convection and conduction coefficients, and the values that best reproduce the measured cooldown profiles are selected for subsequent DED simulations.

The calibration results, shown in Fig. 5, indicate that a surface film coefficient of 9 W/(m^2 K) adequately represents free convection, while 500 W/(m^2 K) corresponds to conductive heat transfer to the mounting frame. Thermal radiation is included in both simulations using the calibrated emissivity and an ambient temperature of 298 K. The calibrated boundary condition parameters, summarised in Table 5, are applied consistently throughout the subsequent numerical case studies.

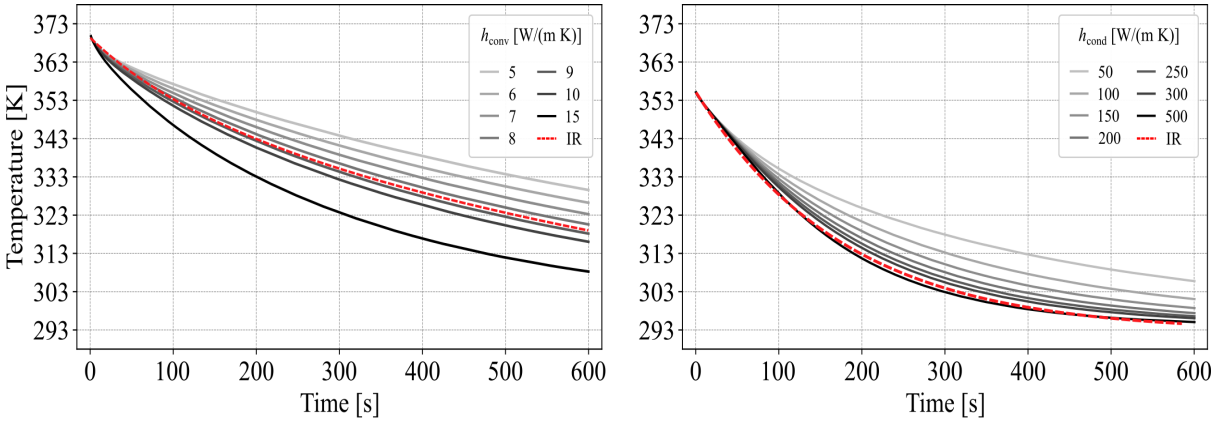

(a) Free convection (b) Conduction

Fig. 5. Experimental (IR) and computed temperature histories at the substrate centre for (a) free convection boundary conditions and (b) conductive heat transfer to the mounting frame.

Table 5. Calibrated thermal boundary condition parameters used in the numerical case studies.

Parameter	Symbol	Value
Ambient temperature [K]	T_∞	298.0
Cold water temperature [K]	T_{base}	292.0
Convective film coefficient [W/(m^2 K)]	h_{conv}	9.0
Contact film coefficient [W/(m^2 K)]	h_{cond}	500.0
Substrate surface emissivity [/]	ε_{sub}	0.3
Speckle pattern surface emissivity [/]	ε_{DIC}	0.9

Mechanical boundary conditions.

In the mechanical analysis, the interaction between the substrate, clamping brackets, and mounting frame is captured through surface contact, combined with the compliance of the screw connections. Rather than prescribing fixed supports, the flexibility of each screwed joint is represented using axial springs with a stiffness of 5000 N/mm. These springs are attached to reference points (RP) associated with the washer regions beneath the screws, as shown in Fig. 4.

Contact interactions use hard pressure-overclosure behaviour and penalty friction with a coefficient of 0.3. Gravity is included in all simulations. The mounting frame is fully fixed, while each clamping bracket is permitted to rotate about its outer edge, effectively acting as a hinge. As a result, the substrate is constrained only through these contact regions, with no additional boundary conditions applied.

Results and Discussion

Thermal model validation.

To evaluate the thermal model, numerically predicted temperature fields are compared with IR-camera measurements for the unidirectional deposition case. Three representative monitoring points on the underside of the substrate, located beneath the first, middle, and last cladding paths, are selected for direct comparison with corresponding numerical nodes, as shown in Fig. 6a-c.

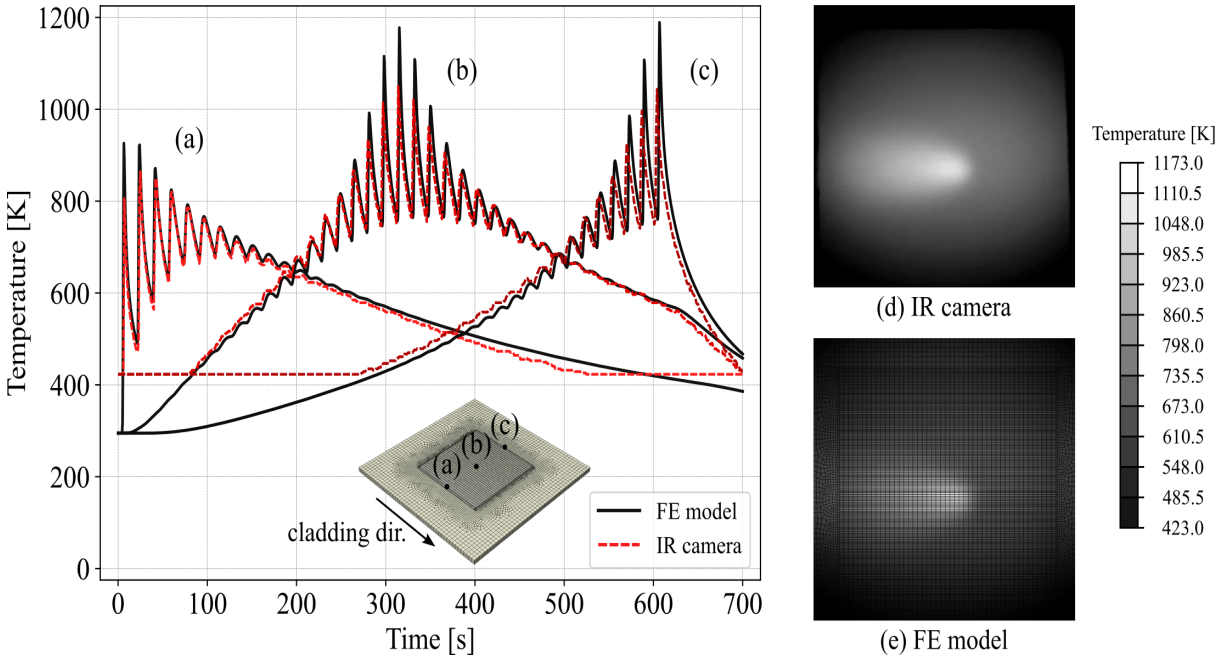

Fig. 6. Simulated (black) and measured (red) temperature histories on the bottom surface for the unidirectional deposition path beneath the: (a) first bead, (b) middle bead, and (c) last bead. The right-hand side shows corresponding bottom surface temperature fields during deposition obtained from: (d) IR measurements and (e) numerical simulation.

The model captures the overall thermal evolution with good agreement. The mean difference between measured and predicted temperatures is approximately 4.8 K, with the largest deviations occurring near peak temperatures due to IR-camera resolution limits and minor timing offsets. Spatial comparisons of full-field temperature distributions, shown in Fig. 6d-e, further confirm the consistency between simulation and experiment, supporting the validity of the thermal model for subsequent thermo-mechanical analyses.

Mechanical model validation.

The mechanical model is assessed by comparing simulated vertical displacements for the unidirectional deposition case with in situ measurements obtained from the stereo DIC system. Fig. 7a-c shows the temporal evolution of out-of-plane deformation along a representative cross section during deposition, and Fig. 7d presents the final deformations after cooling and unclamping. Numerical predictions reproduce the main displacement patterns during deposition and match the experimental observations well within the DIC measurement region.

Larger discrepancies appear toward the end of the process, which can be attributed to the use of an isotropic hardening model and simplifications in the clamping representation. These effects cause the model to respond slightly too stiffly during deposition and to overestimate deformation after cooling and unclamping. Before unclamping, the maximum error between the numerical and experimental results reaches 0.328 mm, and after unclamping the release of residual stresses increases the discrepancy to a maximum of 0.520 mm. Despite these deviations, the simulated displacement evolution follows the experimental trends closely, and the comparison of full-field displacement field in Fig. 7e-f confirms that the thermo-mechanical model provides sufficiently accurate predictions for further analysis.

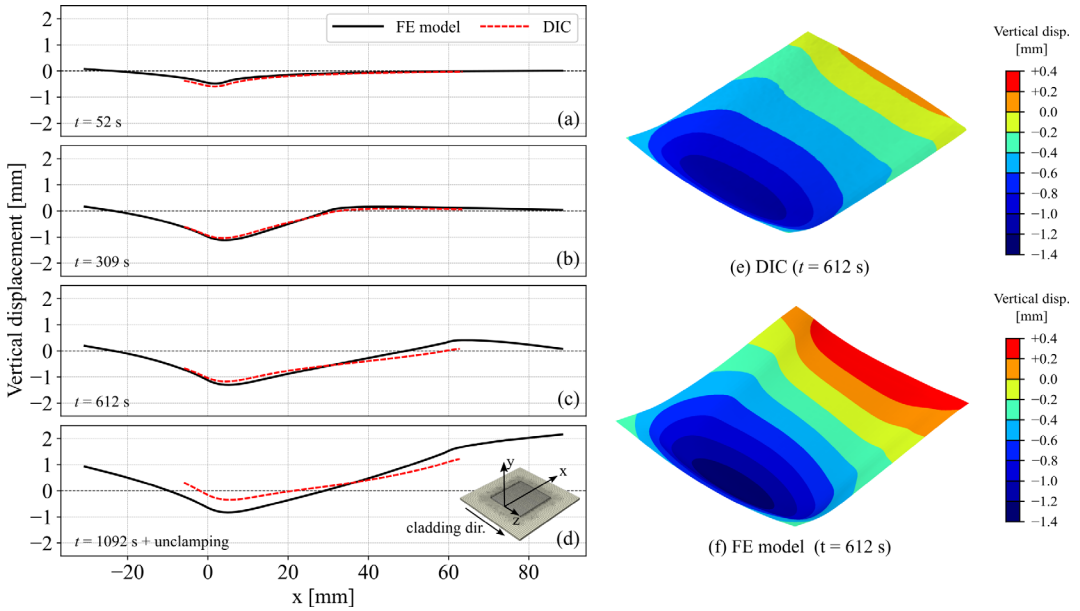

Fig. 7. Simulated (black) and measured (red) substrate vertical displacement profiles for the unidirectional deposition path at the end of the: (a) third bead, (b) middle bead, and (c) last bead. Subfigure (d) shows the substrate displacement profile after cooldown and unclamping. The right-hand side shows corresponding bottom surface displacement fields at the end of deposition before unclamping obtained from (e) stereo DIC measurements and (f) numerical simulation.

Influence of deposition pattern on residual stresses and substrate deformation.

The validated model is applied to compare three toolpath layouts: unidirectional, bidirectional and inward spiral. Fig. 8 presents the resulting vertical deformation of the substrate bottom surface before and after unclamping. The inward-spiral strategy leads to the lowest overall deformation and exhibits minimal springback after release, whereas both linear strategies show noticeably larger deformation and more pronounced springback.

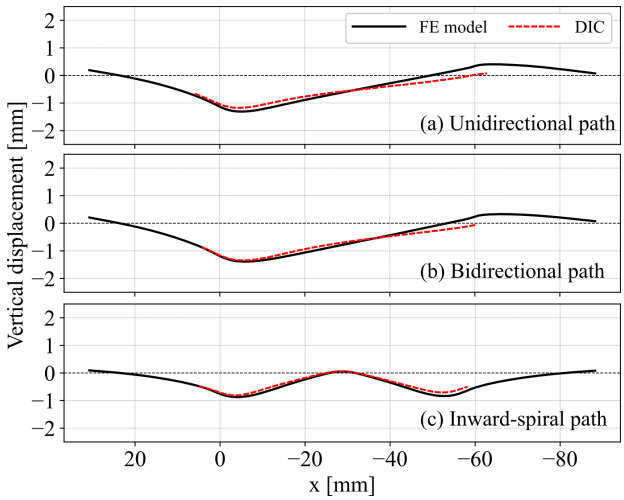

Fig. 8. Simulated (black) and measured (red) vertical displacement profiles of the substrate at room temperature before unclamping for the: (a) unidirectional, (b) bidirectional, and (c) inward spiral deposition paths.

The evolution of the maximum vertical displacement during deposition is shown in Fig. 9, where the reported values represent the maximum within the DIC measurement area. The bidirectional strategy results in the largest displacement, reaching approximately 1.30 mm, followed by the unidirectional case with about 1.15 mm, while the inward-spiral path limits the displacement to 0.81 mm. The numerical model slightly overpredicts the final peak values by up to 0.166 mm (14.4%) for the unidirectional, 0.082 mm (6.3%) for the bidirectional and 0.065 mm (8.0%) for the spiral strategy.

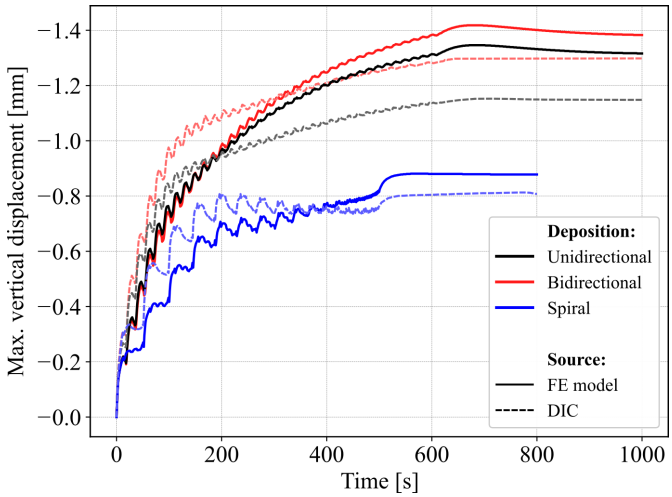

Fig. 9. Maximum substrate displacement history during unidirectional (black), bidirectional (red) and inward spiral (blue) cladding. Solid lines denote numerical simulation results, while dashed lines of the same colour indicate DIC measurements.

Conclusion

This study presents a thermo-mechanical FE framework for DED, together with an in-situ validation setup that combines IR thermography and stereo DIC, enabling continuous full-field monitoring of temperature and deformation on the underside of the substrate. The calibrated model reproduces the measured thermal and mechanical behaviour with good accuracy and highlights the importance of realistic boundary conditions. The simulation results show that the inward-spiral deposition strategy yields the smallest distortions, whereas linear paths produce larger deflections and more pronounced springback.

Acknowledgement

The authors acknowledge the financial support of the Slovenian Research Agency (research core funding No. P2-0263 and No. N2-0328).

References

[1] X. Bai, H. Zhang, G. Wang, Improving prediction accuracy of thermal analysis for weld-based additive manufacturing by calibrating input parameters using IR imaging, Int J Adv Manuf Technol 69 (2013), pp. 1087–1095.

[2] J.C. Heigel, P. Michaleris, E.W. Reutzel, Thermo-mechanical model development and validation of directed energy deposition additive manufacturing of Ti–6Al–4V, Addit. Manuf. 5 (2015), pp. 9–19.

[3] Z. Yan, W. Liu, Z. Tang, X. Liu, N. Zhang, M. Li, H. Zhang, Review on thermal analysis in laser-based additive manufacturing, Opt. Laser Technol 106 (2018), pp. 427–441.

[4] M. Pratt, H. Mirmohammad, O. Kingstedt, T. Ameel, S. Rao, High-speed bottom-up surface temperature measurements of a flat plate: A thermal analog for laser metal additive manufacturing, J. Manuf. Process. 122 (2024), pp. 65–82.

[5] P. Li, J. Liu, J. Zhou, A. Feng, Y. Gong, J. Lu, X. Meng, In-situ and off-line deformations of cylindrical walls manufactured by directed energy deposition with different dwell times, Measurement 198 (2022), 111402.

[6] F. G. Cunha, T. G. Santos, J. Xavier, In Situ Monitoring of Additive Manufacturing Using Digital Image Correlation: A Review, Mater. 14 (2021), 1511.

[7] B. Starman, T. Pepelnjak, A. Maček, M. Halilovič, S. Coppieters, Inverse calibration of out-of-plane shear anisotropy parameters of sheet metal, Int. J. Solids Struct. 313 (2025), 113313.

[8] Š. Obid, B. Starman, J. Urevc, M. Halilovič, Extraction of uniaxial stress–strain curve from bending test using DIC measurements, Eur. J. Mech. A-Solid. 106 (2024), 105346.

[9] Q. Wang, J. Jia, Y. Zhao, A. Wu, In situ measurement of full-field deformation for arc-based directed energy deposition via digital image correlation technology, Addit. Manuf. 72 (2023), 103635.

[10] D. Kovšca, B. Starman, D. Klobčar, M. Halilovič, N. Mole, Towards an automated framework for the finite element computational modelling of directed energy deposition, Finite Elem. Anal. Des. 221 (2023), 103949.

[11] P. Michaleris, Modeling metal deposition in heat transfer analyses of additive manufacturing processes, Finite Elem. Anal. Des. 86 (2014), pp. 51–60.

[12] O. Muránsky, C.J. Hamelin, M.C. Smith, P.J. Bendeich, L. Edwards, The effect of plasticity theory on predicted residual stress fields in numerical weld analyses, Comput. Mater. Sci. 54 (2012), pp. 125–134.

[13] A. Santi, M. Bayat, V. K. Nadimpalli, A. Fabrizi, F. Bonollo, J. H. Hattel, Validation of an experimentally-based heat source for flash heating modeling of directed energy deposition: Systematic study of process and simulation parameters, J. Manuf. Process. 121 (2024), pp. 35–50.

[14] J. Goldak, A. Chakravarti, M. Bibby, A new finite element model for welding heat sources, Metall. Trans. B 15 (1984), pp. 299–305.